NANO · MICRO small
www.small-journal.com

Structural Effects of 3D Inkjet-Printed Ni(O)-YSZ Pillared Electrodes on Performances of Solid Oxide Electrochemical Reactors

Inyoung Jang, Anna Hankin, Zheng Xie, Stephen J. Skinner, and Geoff H. Kelsall*

Increasing densities of reaction sites for gaseous reactants in solid oxide electrochemical reactors (SOERs), is a key strategy for achieving enhanced performance in either fuel cell or electrolysis modes. Fabrication of 3D structured components in SOERs can enhance those densities of reaction sites, which is achieved by 3D inkjet printing with high reproducibility, having developed inks with appropriate properties. First, the effects of pillar geometries on SOER performances are predicted through numerical simulations, enabling subsequent 3D printing to focus on the more effective geometries. Herein, the study reports the results of experimental validation of those predictions by evaluating the electrochemical performances of cells with various heights of 3D inkjet-printed Ni(O)- yttria stabilized zirconia (YSZ) pillars and YSZ pillars. Those measurements prove that increasing pillar heights generally increases SOER peak power densities in fuel cell mode and increased current densities at the thermoneutral potential (1.285 V) in steam electrolysis mode, as predicted by simulations. With increasing pillar heights, more limitations in performance enhancement are found with YSZ electrolyte pillars than with Ni-YSZ pillars, again as predicted by simulations. The subsequent microstructural analysis of Ni-YSZ pillars proves the suitability of the Ni(O)-YSZ composite particle ink formulation and the reliability of 3D printing.

1. Introduction

Solid oxide electrochemical reactors (SOERs) are one of the most promising energy conversion systems for sustainable fuel production (in electrolyzer mode with renewable energy sources; SOE) and utilization (fuel cell mode: SOFC), thereby contributing to achieving a net-zero society.[1] Their high operating temperatures enable them to achieve amongst the highest electrical energy conversion efficiencies of 60–70%, depending on current density.[2] SOEs enable energy storage, e.g. in the chemical energy of H_2, CO, etc., subsequent reconversion of which to electrical energy in SOFCs could address inherent intermittencies of renewable energy systems, decarbonize electrical power generation, and better balance electrical power supply and demand.[3]

Amongst the various strategies for fabricating high-performance SOERs, one approach is to increase specific interfacial areas between electrode and electrolyte layers, e.g., constructing 3D structured SOERs.[4] Forming 3D structured nickel oxide (Ni(O))-yttria stabilized zirconia (YSZ) layers could achieve this objective, and may be preferred to 3D structured electrolyte layers, as thicker electrolyte layers cause increased ohmic potential drops and more inhomogeneous current density distributions.[5] (**Figure 1a**)

Finite element simulations of the effects of Ni(O)-YSZ geometries on reactor electrochemical behavior were reported previously,[4b] predicting much-enhanced performance of Ni(O)-YSZ pillar structured cells when pillar heights were increased. (Figure S1a, Supporting Information) The simulation results have been replotted in Figure 1b, by dividing the current by the total, rather than geometric / cross-sectional, surface area of electrodes. For fuel cell mode, power densities were predicted to increase with pillar heights up to ≈70 µm, due to the increased triple phase boundary (TPB) densities in pillared structures. For pillar heights >70 µm, power densities were predicted to decrease with increasing pillar height, due to depletion of gas reactant inside pillars, causing their uppermost parts to become inactive. In electrolysis mode with just 20% H_2O fed to negative electrodes, current densities at the thermoneutral potential difference decreased with increasing pillar height, and steam reactant depletion caused potential-current (*U-j*) gradients to become steeper. When the pillar diameter was 5 µm, gas transport through the

I. Jang, A. Hankin, G. H. Kelsall
Department of Chemical Engineering
Imperial College London
Exhibition Rd, London SW7 2AZ, UK
E-mail: i.jang@imperial.ac.uk
Z. Xie, S. J. Skinner
Department of Materials
Imperial College London
Exhibition Rd, London SW7 2AZ, UK

The ORCID identification number(s) for the author(s) of this article can be found under https://doi.org/10.1002/smll.202306653

© 2024 The Authors. Small published by Wiley-VCH GmbH. This is an open access article under the terms of the Creative Commons Attribution License, which permits use, distribution and reproduction in any medium, provided the original work is properly cited.

DOI: 10.1002/smll.202306653

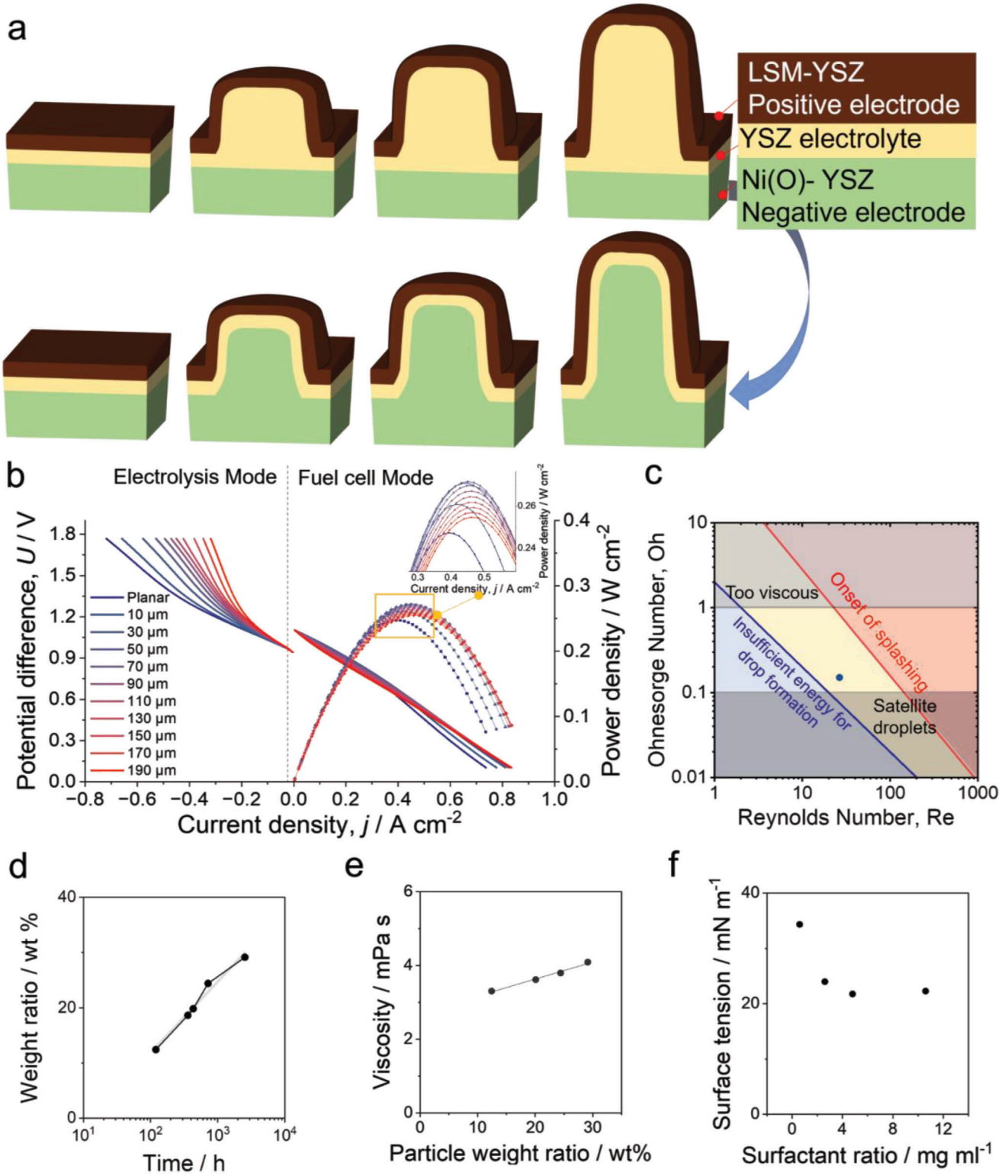


Figure 1. a) Schematic illustration of the Ni(O)-YSZ pillared structured SOERs with various heights of pillars. b) Predicted SOER performances in both fuel cell and electrolysis modes as predicted by COMSOL Multiphysics simulation. Replotted from the reference with permission.[4b] c) The ink property diagram plotted based on suitable ink printing conditions for inkjet printing: $We^2 > 4$, $Oh\,Re^{5/4} < 50$, and $1 < Z < 10$. Reproduced with permission.[6] d) Effect of ball milling time on ink weight ratio. Effect of particle weight ratio in ink, on ink viscosity. f) Effect of surfactant concentration on surface tension.

© 2024 The Authors. Small published by Wiley-VCH GmbH

16136829, 2024, 40, Downloaded from https://onlinelibrary.wiley.com/doi/10.1002/smll.202306653 by Imperial College London, Wiley Online Library on [22/10/2024]. See the Terms and Conditions (https://onlinelibrary.wiley.com/terms-and-conditions) on Wiley Online Library for rules of use; OA articles are governed by the applicable Creative Commons License

porous pillar structure became more limiting, leading to more severe reactant depletion within pillar structures (Figure S1b, Supporting Information).

Reactors with ionically-conducting YSZ pillars showed more limited increase in peak power densities with increasing pillar height, compared to the electronically-conducting Ni(O)-YSZ pillar behavior, due to increased path lengths of oxygen ions in the YSZ, causing increased ohmic potential drops. Hence, the maximum power density enhancement factor was 1.9 (Figure S1c, Supporting Information) compared with 4.9 for reactors with Ni(O)-YSZ pillars.

The objectives of the work for which results are reported herein were to validate experimentally the computational predictions of SOFC and SOE electrochemical performances with Ni(O)-YSZ and YSZ pillar heights, fabricated by controlling the numbers of printed layers in inkjet 3D printing (Figure 1a). To isolate those effects, additional functional layers, YSZ electrolyte on Ni(O)-YSZ pillars, and lanthanum strontium manganite (LSM)-YSZ positive electrodes, were deposited by dip-coating, which unfortunately produced spatially inhomogeneous distributions.

As an additional interpretational aid, microstructures of 3D printed Ni-YSZ pillars were analyzed by focused ion beam-scanning electron microscopy (FIB-SEM) tomography, to obtain the physical/chemical information of pillar structures and to confirm their homogeneity in Ni-YSZ composite microstructures fabricated using 3D inkjet printing. Using the parameters obtained by 3D tomography, supplementary computational simulations were conducted to provide more realistic predictions of reactor performance, as reported in the Supporting Information.

2. Results and Discussion

2.1. Ink Property Characterisation and 3D Ink-Jet Printing

Several physical parameters need to be considered in preparing stable particulate dispersions for consistent inkjet printing, such as ink density (u_o), droplet ejection velocity, the characteristic length (r, diameter of printer nozzle), ink viscosity (η) and surface tension of the ink (γ). The printability of inks can be evaluated typically by three dimensionless numbers derived using their physical parameters: Reynolds (Re), Weber (We), and Ohnesorge numbers (Oh), defined by Equations (1)–(3).[7] Typically, inks are considered printable when their Z values (Oh^{-1}) are between 1 and 10[8] or 4 and 14.[9]

$$\mathrm{Re} = \frac{\rho u_0 r}{\eta} \tag{1}$$

$$\mathrm{We} = \frac{u_0^2 \rho r}{\gamma} \tag{2}$$

$$\mathrm{Oh} = \frac{\sqrt{\mathrm{We}}}{\mathrm{Re}} = \frac{\eta}{\sqrt{\gamma \rho r}} \tag{3}$$

The Re–Oh number diagram is replotted in Figure 1c to confirm the ink formulated for 3D printing was within the printable area (Yellow color). Based on the stable operation of drop-on-demand inkjet printing conditions reported previously, the formulated NiO-YSZ ink should fit the following conditions: $1 < Z < 10$ for suitable ink viscosity for printing, $We^2 > 4$ for a drop to possess sufficient energy to be ejected, and $Oh\ Re^{5/4} < 50$ to avoid onset of splashing.[6,10]

To calculate the dimensionless numbers and fit the required conditions, several ink property analyses were conducted along with the adjustment of ink density, viscosity, ball-milling time, surfactant ratio, and dispersant ratio. The effects of dispersant ratio on zeta potential values and average particle sizes in the solvent are shown in Figure S2 (Supporting Information). As shown in Figure S3 (Supporting Information), increasing ball milling time decreased NiO-YSZ particle sizes significantly, with a limiting effect after ca. 100 h. The use of the right dispersant ratio had led to the earlier saturation of particle size and adding a sonification process accelerated the saturation of particle size.

Since the dispersed particle size decreased as the ball milling time increased, a larger number of particles remained after filtration, thereby the weight ratio of the ink increased linearly with ball milling time in a log scale (Figure 1d). Through the process, the ink weight ratio has been controlled and viscosity increased linearly to the ink weight ratio (Figure 1f). All the viscosity values fit into the range from 1 to 25 mPa s which would be recommended for the inkjet printing.[11] Here, the particle weight ratio was fixed to 13 wt.% considering the time required for ink preparation. Surfactant was added for increasing the stability of the ink dispersion property as a final step, and the ratio of surfactant varied from 0.5 to 10 mg to the volume of ink (ml) to find a suitable surface tension value when the particle weight ratio has been fixed to 13 wt.%. The surfactant ratio of 2.5 mg cm^{-3} was chosen, considering the general recommended surface tension range for inkjet printing and corresponding Oh and Re values.[9,11] The dimensionless values were calculated based on the physical/chemical parameters of the ink with the optimized additive ratios and the size of the nozzle used for the printing was 19–20 µm (DMC, Fujifilm, Japan). The ink has the Oh value of 0.143, Re value of 27.05, and Z (Oh^{-1}) of 7.01, which are all suitable values for inkjet printing, staying in the yellow area in the plot (Figure 1c). The ink for YSZ pillar printing was already reproducible and well-studied and developed in the previously published work, so is not discussed further in this manuscript.[12]

Using the formulated ink, 3D pillared structures were inkjet printed by layer-by-layer printing circular shapes, as illustrated schematically in Figure S4a (Supporting Information). Figure S4b (Supporting Information) shows the first printed layer of Ni(O)-YSZ layer, formed by droplets of Ni(O)-YSZ printed in a circular shape, with the pillar height controlled by the number of layers printed.

2.2. Effect of YSZ Electrolyte Pillar Heights on SOFC Performances

To validate the effects of pillar height on SOFC and SOE performances predicted by computational simulations, YSZ pillars were printed with various heights (ca. 20–100 µm) by controlling the number of printed layers (20-100). Figure S5

© 2024 The Authors. Small published by Wiley-VCH GmbH

RIGHTSLINK
16136829, 2024, 40, Downloaded from https://onlinelibrary.wiley.com/doi/10.1002/smll.202306653 by Imperial College London, Wiley Online Library on [22/10/2024]. See the Terms and Conditions (https://onlinelibrary.wiley.com/terms-and-conditions) on Wiley Online Library for rules of use; OA articles are governed by the applicable Creative Commons License

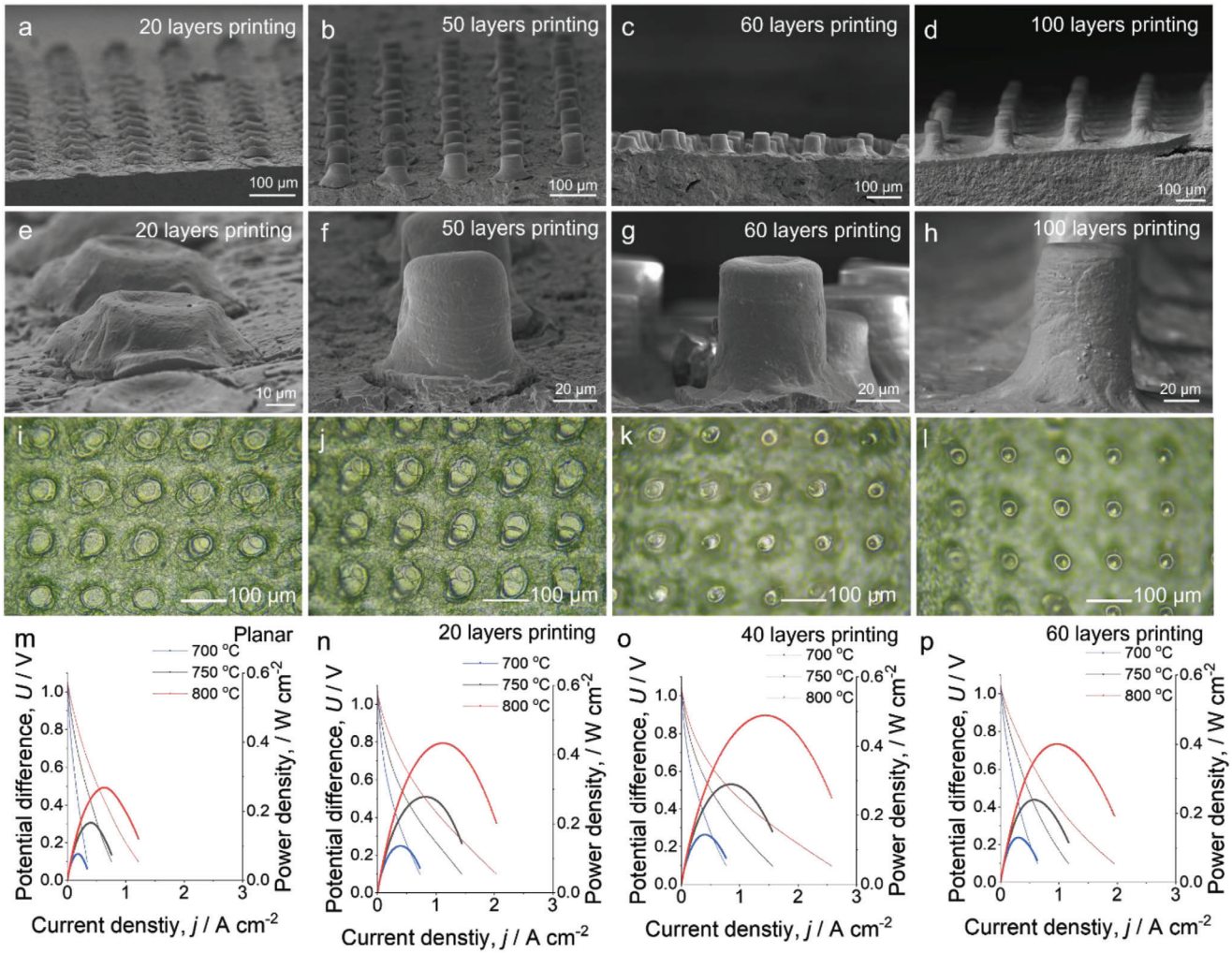


Figure 2. a–d) SEM images of printed and sintered YSZ pillars at lower (a–d) and higher (e–h) magnification, after 20, 50, 60, and 100 printed layers. i–l) Top view optical microscope (OM) images of YSZ pillars after sintering, and: i) 20, j) 40, k) 60 and l) 80 layers printing). m–p) Effect of current density on SOFC potential differences and power densities at 700, 750, and 800 °C, with 0, 20, 40, and 60 printed layers of YSZ pillars.

(Supporting Information) shows optical microscope (OM) images of those YSZ pillars immediately after printing. For comparison, **Figure** 2a–h shows SEM images of pillar microstructures after sintering at 1450 °C for 5 h. The number of printed layers (20, 50, 60, 100) produced the expected corresponding increase in heights of post-sintered YSZ pillars of 20, 50, 60, and 90–100 µm, as shown in Figure 2e–h. LSM-YSZ positive electrode layers were dip-coated on YSZ pillar surfaces, then sintered at 1000 °C for 2 h, so forming complete fuel cells, the performances of which were determined subsequently, as shown in Figure 2m–p.

Figure 2m–p shows the effects of current density and YSZ electrolyte pillar height on SOFC potential differences and power densities at 700, 750, and 800 °C. As shown in the potential-current density- power density (*U-j-P)* plots, peak power densities increased with pillar height, but reached a maximum value for a pillar height of 40 µm, and then decreased slightly for a pillar height of 60 µm. Cross-sectional images of the post-service cells used to determine the data in Figure 2m–p are shown in Figure S6 (Supporting Information). It can also be noted that the surface of the YSZ pillars became rougher with increasing numbers of printed layers. This is evident in the SEM images of YSZ pillars in Figure 2e–h, displaying the detailed microstructure of the pillars' front view. The increased roughness of the surface, correlating with pillar heights, could be due to a higher probability of ink splashing with increased printing time. Figure S6h (Supporting Information) shows that the top part of the 60 µm pillar was not fully covered by the LSM-YSZ positive electrode layer, so explaining why peak power densities were less for the 60 µm high pillars than for 40 µm high pillars, despite the latter's smaller electrolyte specific surface area. The exposed YSZ is more obvious in the top view SEM image of the post-tested pillars shown in Figure S7 (Supporting Information). The exposure of the surface possibly occurred during the drying process. After dip-coating the LSM-YSZ layer, the cell was placed horizontally, causing the ink to flow downward while drying. This led to the exposure or an excessively thin LSM-YSZ layer on the top. The exposed top surface was also observed in the Ni(O)-YSZ pillar structures, which will be discussed in Section 2.5.

© 2024 The Authors. Small published by Wiley-VCH GmbH
RIGHTSLINK
16136829, 2024, 40, Downloaded from https://onlinelibrary.wiley.com/doi/10.1002/smll.202306653 by Imperial College London, Wiley Online Library on [22/10/2024]. See the Terms and Conditions (https://onlinelibrary.wiley.com/terms-and-conditions) on Wiley Online Library for rules of use; OA articles are governed by the applicable Creative Commons License

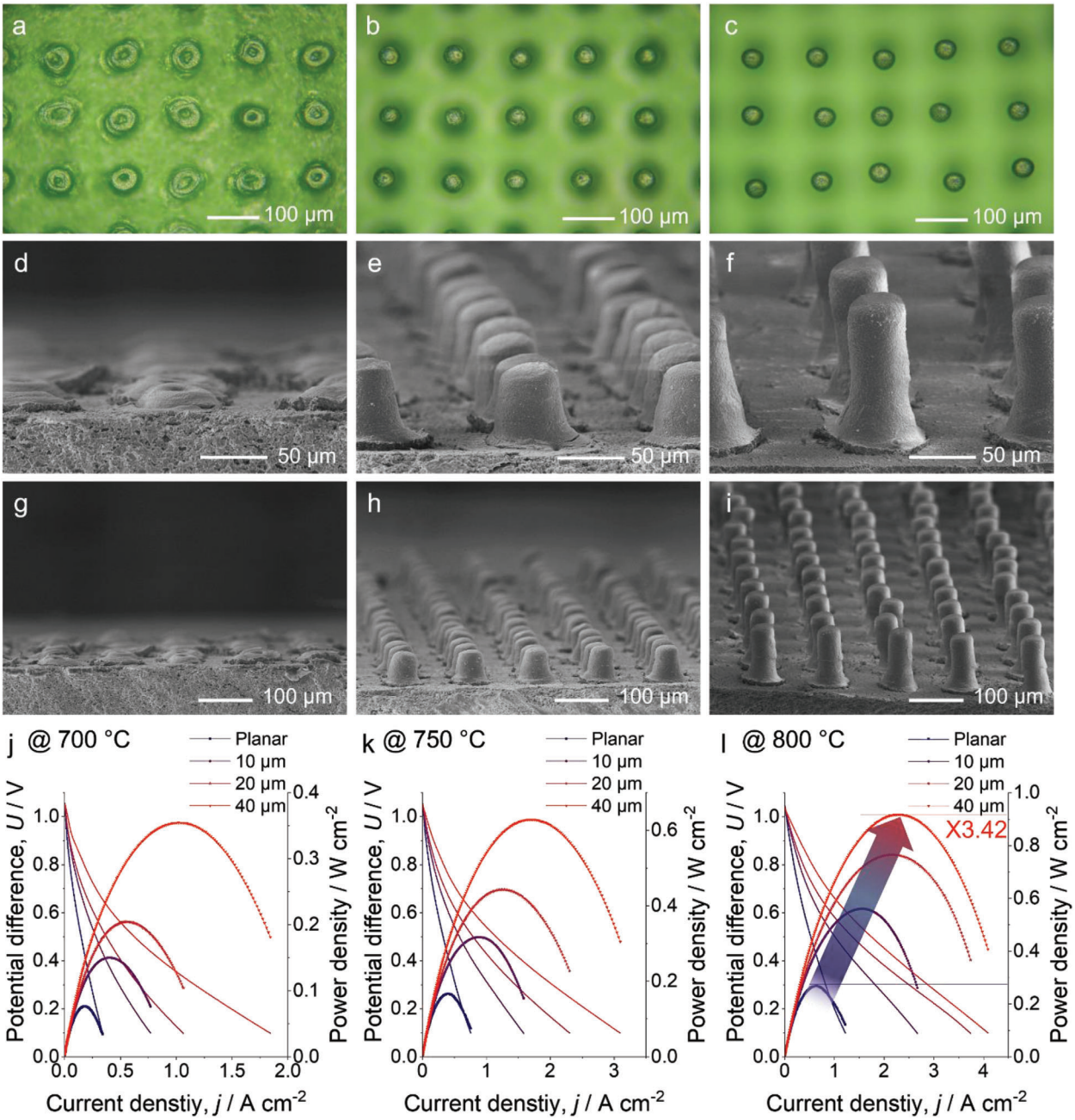


Figure 3. a–c) Top-view optical microscopic (OM) images of Ni(O)-YSZ pillars after sintering of a) 40, b) 80, and c) 120 printed layers. d–f) cross-sectional SEM images of the same Ni(O)-YSZ pillars at higher magnification and g–i) lower magnification. Measured effects of current density and 10, 20, and 40 µm pillar heights, on cell potential differences (*U*) and power densities (*P*) at j) 700 °C, k) 750 °C, and l) 800 °C.

2.3. Effect of Ni(O)-YSZ Pillar Heights on SOFC Performances

Figure S8a–c (Supporting Information) show printed Ni(O)-YSZ pillars immediately after printing, their brown color being that of slightly sub-stoichiometric nanoparticulate NiO in the NiO-YSZ particulate composite ink. After sintering the pillars at 1450 °C for 5 h, the color changed to green as shown in **Figure 3**a–c, due to the change in stoichiometry and NiO particle size growth during sintering.[13] Figure S9 (Supporting Information) shows the top-view SEM images of the same samples, with Figure S10 (Supporting Information) showing lower magnification top-view images of homogeneous printed pillar arrays without missing pillars.

Figure 3d–f show cross-sectional microstructural SEM images of Ni(O)-YSZ pillars with higher magnification, with lower magnification images of greater numbers of pillars in Figure 3g,h. In the OM & SEM images of pillars with 40 printed layers (Figure 3a,d), the coffee stain effect was evident,[14] but it disappeared on printing of additional layers, as evident from the images of 80 and 120 printed layers. The coffee stain effect is caused

© 2024 The Authors. Small published by Wiley-VCH GmbH

16136829, 2024, 40, Downloaded from https://onlinelibrary.wiley.com/doi/10.1002/smll.202306653 by Imperial College London, Wiley Online Library on [22/10/2024]. See the Terms and Conditions (https://onlinelibrary.wiley.com/terms-and-conditions) on Wiley Online Library for rules of use; OA articles are governed by the applicable Creative Commons License

by faster evaporation rates at the edges and centers of a droplets, causing gradients in surface tension. The appearance of the coffee stain effect in the first 40 layers and its subsequent disappearance could be due to the change in affinity, moving from the interaction between NiO-YSZ ink and the surface of substrate, to that between NiO-YSZ ink and the printed Ni(O)-YSZ, thereby altering the degree of Marangoni flow within the droplet.[15]

Figure 3j-l shows the effects of current density and pillar height (10, 20, and 40 µm), on fuel cell potential differences (*U*) and power densities (*P*) at 700 °C (Figure 3j), at 750 °C (Figure 3k) and at 800 °C(Figure 3l), increasing pillar heights generally enhancing performance. Whereas the peak power density (PPD) for the planar cell operating at 800 °C was 268 mW cm^{-2}, that for the cell with 40 µm Ni(O)-YSZ pillars was 913 mW cm^{-2}, corresponding to an enhancement factor of 3.4. For comparison, the PPD of a cell with 40 µm YSZ pillars was 489 mW cm^{-2}, corresponding to the much lower enhancement factor of 1.82, as predicted by computational simulation.[5] The experimental Ni(O)-YSZ pillar heights used were much shorter than the maximum value of the range covered in the COMSOL simulation, due to the practical difficulty of forming an electrolyte layer, as explained in Section 2.5. The EIS data for cells operating at 700, 750, and 800 °C with 0, 10, 20, 40 µm Ni(O)-YSZ pillars are shown in Figure S11 (Supporting Information); corresponding R_{ohm} and R_p values are in Table S1 (Supporting Information).

2.4. Solid Oxide Electrolyser (SOE) Performance Characterization

The electrolysis performances of cells with Ni(O)-YSZ pillars were evaluated both for steam (**Figure 4a**) and CO_2 (Figure 4b) electrolysis. In steam electrolysis at 800 °C, current densities were enhanced by the presence of 40 µm pillars by a factor of ca. 2 at the thermoneutral potential of 1.285 V,[16] in good agreement with computational simulations shown in Figure 4c. For easier comparison, both sets of data are plotted on one graph in Figure S12 (Supporting Information). When current densities were compared at the thermoneutral potential of 1.464 V at 750 °C,[17] a similar enhancement factor due to 40 µm high pillars was achieved in CO_2 electrolysis at 750 °C with a CO_2 flow of 70 standard cubic centimeters per minute (sccm) and CO flow of 30 sccm to the negative Ni(O)-YSZ electrode. Though magnitudes of current densities were smaller for those for steam electrolysis, the former process having slower kinetics, the current density enhancement for pillared negative electrodes again demonstrated benefits for CO_2 electrolysis as well.[18]

Effects of current densities (*j*), pillar heights, and temperature (700, 750, and 800 °C) on potential differences (*U*) for steam electrolysis, and of pillar heights and gas compositions for CO_2 electrolysis at 750 °C, are reported in Figures S13 and S14 (Supporting Information), respectively.

Figure 4d–g respectively show cross-sectional SEM images of the cells with ca. 0, 10, 20, and 40 µm pillar heights used in these experiments. The practical problem of dip-coating YSZ layers onto the taller Ni(O)-YSZ electrode pillars >80 µm and especially 160 µm, caused them to exhibit electrochemical performances lower than predicted, for microstructural reasons explained below.

2.5. Microstructural Analysis of Ni(O)-YSZ Pillar Structures

Fabrication of full cells with taller Ni(O)-YSZ pillars led to several practical difficulties for evaluating their electrochemical performances. First, when YSZ electrolyte layers were coated on Ni(O)-YSZ surfaces by dip-coating on pillars > 80 µm high, YSZ layers on top surfaces of pillars tended not to be thick enough to prevent pinholes, as shown in the **Figure 5a**. Figure S15 (Supporting Information) shows more detail of the cross-sectional microstructures of the pillars with ca. 80 and 160 µm heights, cut by focused ion beam. Normally, for coating of ca. 7 µm YSZ electrolyte layers on negative electrode support substrates, single dip-coating is required.[12,19] However, even after repeating the dip-coating three times on 160 µm high pillar structures, several pillars still showed the brown color of Ni(O)-YSZ on the top part of pillars; this is evident from the top-view OM images of pillars in Figure S16 (Supporting Information).

SEM images of Ni-YSZ pillar microstructures after sintering showed cracks between pillars (Figure 5a; Figure S17, Supporting Information), and the top part of pillars had YSZ thicknesses of only 1–2 µm (Figure S17b, Supporting Information), compared with almost 20 µm on the lowest part of pillars (Figure S17a, Supporting Information). Ideally, YSZ layers should be coated conformally on Ni(O)-YSZ pillar surfaces, as shown schematically in Figure S18a (Supporting Information). However, dip-coating led to uneven YSZ thicknesses as shown in Figure S18b (Supporting Information), which resulted in the cracks shown in the cross-sectional image of the cell. Differences in layer thicknesses coated on bottom and top parts of pillars were caused by differences in capillary suction pressures, due to differences in porosities of substrate and pillar structures;[20] surface porosities of substrates are well known to greatly affect thicknesses of dip-coated layers.[21]

Porosities of Ni(O)-YSZ pillars were expected to be very low, as the pillars contained no pore-former and NiO had yet to be reduced to Ni, contrary to Ni(O)-YSZ substrates that had high porosity after combustion of pore-formers. Most porosity in Ni-YSZ pillar structures would have arisen from reduction of NiO to Ni as shown in Figure 5b,c; the lighter colored phase in Figure 5c corresponds to Ni from reduction of NiO, causing porosity. Comparison of porosity in the Ni-YSZ negative electrode substrate and Ni-YSZ pillar after sintering and reduction is shown in Figure S19 (Supporting Information); note that the pillars are not in presintered status. Hence, using the dip-coating method, there is a limit to achieving conformally coated YSZ layers that can cover NiO-YSZ pillars for taller pillar heights, as there would not be enough capillary force for coating the top part of Ni(O)-YSZ pillar structures when Ni(O)-YSZ pillars and substrates were dipped into YSZ particulate dispersions. In addition to the uneven coating of the YSZ electrolyte layer, the dip-coating process used for the LSM-YSZ layer also caused the exposure of pillar tops as shown in Figure 5a, which is similar to what was observed in the cells with YSZ pillars discussed in Section 2.2.

Another possible reason for the thinner LSM-YSZ layer on the top could have been led by the high current densities during the oxygen evolution reaction (OER) in the electrolysis mode. Under conditions of high current density, deviation in reaction rates at TPBs and Double Phase Boundaries (DPBs) can cause variations in lattice parameters, resulting in tensile stresses at the

© 2024 The Authors. Small published by Wiley-VCH GmbH
RIGHTSLINK
16136829, 2024, 40, Downloaded from https://onlinelibrary.wiley.com/doi/10.1002/smll.202306653 by Imperial College London, Wiley Online Library on [22/10/2024]. See the Terms and Conditions (https://onlinelibrary.wiley.com/terms-and-conditions) on Wiley Online Library for rules of use; OA articles are governed by the applicable Creative Commons License

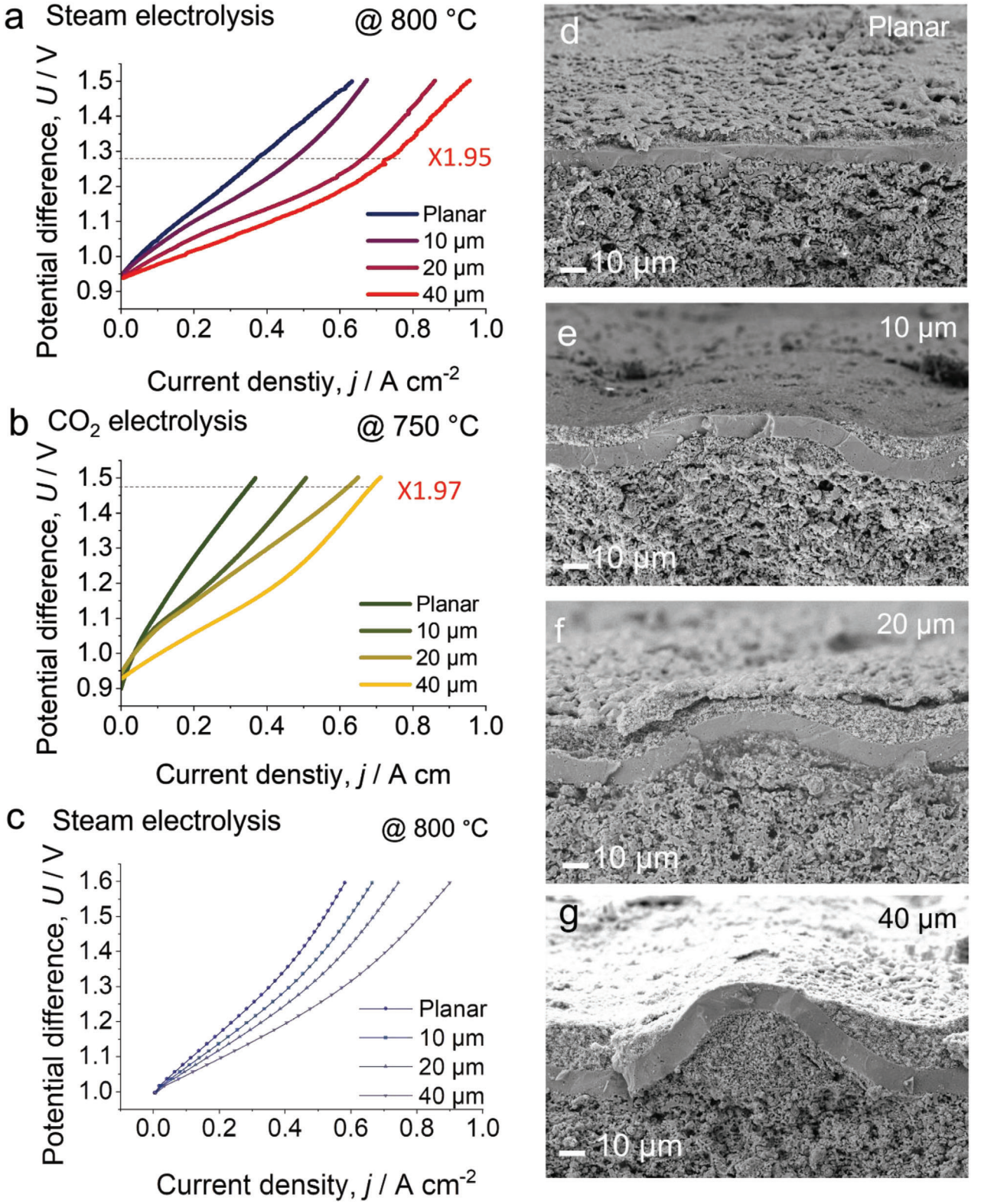


Figure 4. a) Effects of current density (*j*) on potential differences (*U*) for steam electrolysis with cells at 800 °C and 0, 10, 20, 40 μm Ni(O)-YSZ pillar heights. b) Data for CO_2 electrolysis with flow of 70 sccm CO_2 and 30 sccm CO to Ni(O)-YSZ negative electrode with 0, 10, 20, 40 μm pillar heights and cells operating at 750 °C. c) Updated computational simulation of steam electrolysis with cell at 800 °C and 0, 10, 20, 40 μm using the tortuosity value that was obtained from 3D tomography in Section 2.5. Cross-sectional images of cells after experiments. ((d) planar, (e) 10 μm, (f) 20 μm, and (g) 40 μm).

© 2024 The Authors. Small published by Wiley-VCH GmbH
RIGHTSLINK

16136829, 2024, 40, Downloaded from https://onlinelibrary.wiley.com/doi/10.1002/smll.202306653 by Imperial College London, Wiley Online Library on [22/10/2024]. See the Terms and Conditions (https://onlinelibrary.wiley.com/terms-and-conditions) on Wiley Online Library for rules of use; OA articles are governed by the applicable Creative Commons License

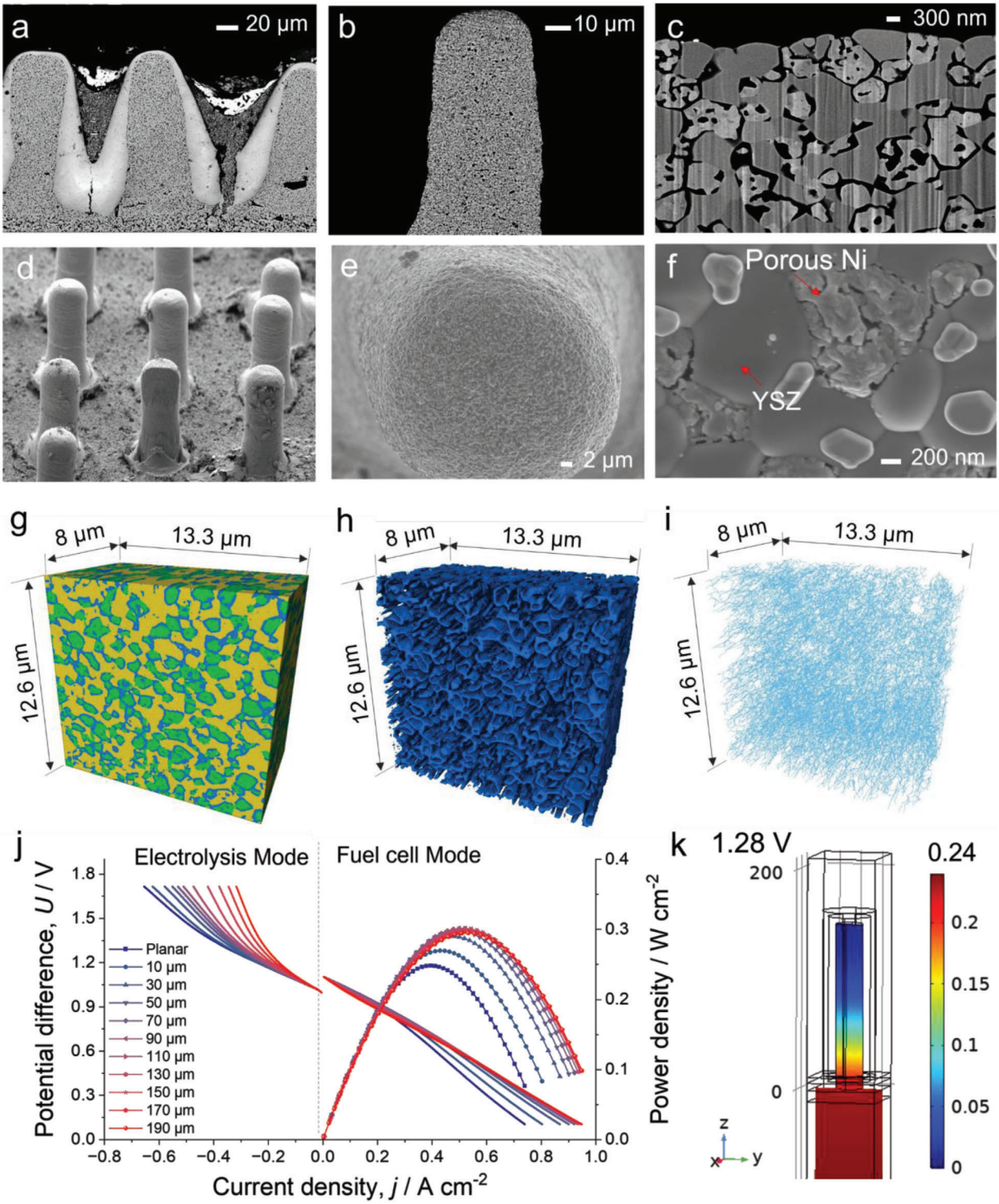


Figure 5. a) Cross-sectional SEM images of a full cell with 160 µm Ni-YSZ pillar height. b) Cross-sectional SEM image of Ni-YSZ pillar after reduction and resin infiltrated. c) Cross-sectional SEM image of top part of Ni-YSZ pillar. (Lighter phase: Ni, grey phase: YSZ) d) SEM image showing Ni-YSZ pillars array used for FIB-SEM 3D tomography. e) SEM image that shows top surface of Ni-YSZ pillar after reduction in H_2 atmosphere at 600 °C. f) Higher magnification of top surface of Ni-YSZ pillar showing porous Ni-YSZ network. g) 3D reconstructed volume analyzed by FIB-SEM 3D tomography. Green, yellow, and blue represent Ni, YSZ, and pore, respectively. h) 3D reconstructed image showing pore distribution in analyzed volume. i) 3D reconstructed image showing distribution of active TPB lengths in analyzed volume. j) Updated computational calculation using the tested cell diameter and the obtained tortuosity value. k) steam distribution through porous Ni-YSZ pillar structure at the thermoneutral potential in electrolysis mode.

© 2024 The Authors. Small published by Wiley-VCH GmbH

16136829, 2024, 40, Downloaded from https://onlinelibrary.wiley.com/doi/10.1002/smll.202306653 by Imperial College London, Wiley Online Library on [22/10/2024]. See the Terms and Conditions (https://onlinelibrary.wiley.com/terms-and-conditions) on Wiley Online Library for rules of use; OA articles are governed by the applicable Creative Commons License

Table 1. Microstructural parameters from FIB-SEM 3D tomography analysis of inkjet printed Ni-YSZ pillars.

Parameters	Values
Pore volume ratio / %	26.9 ± 1.0
YSZ volume ratio / %	47.4 ± 0.1
Ni volume ratio / %	25.7 ± 0.9
Pore tortuosity	1.98 ± 0.02
YSZ tortuosity	1.75 ± 0.03
Ni Tortuosity	15.9 ± 1.0
Total TPB density / μm^{-2}	9.9 ± 0.2
Active TPB density / μm^{-2}	8.2 ± 0.2

layer interfaces.[22] Furthermore, during OER, lattice parameter changes at the air electrode interface due to O^{2-} ion diffusion can also result in the accumulation of tensile strain, likely leading to the delamination of the electrode layer.[23] Therefore, operating the cell under conditions that produce a moderate current densities would be more favorable for reliable operation. However, considering that the cell with SEMs shown in Figure 5a had not been under measurement for an extended period, the reason for the thinner LSM-YSZ layer is more likely to have been caused by the fabrication process.

Additionally, FIB-SEM 3D tomography was used to evaluate the stability of NiO-YSZ inks during the printing process, as the top parts of pillar structures were the last parts printed. After reducing Ni(O)-YSZ pillars to Ni-YSZ, (Figure S20, Supporting Information), the top part of the pillar structure shown in Figure 5d was sliced using a focused ion beam, prior to 3D reconstruction analysis. Prior to FIB-SEM analysis, SEM images of pillar surfaces showed porous Ni networks as shown in Figure 5f. The FIB-SEM tomography was conducted subsequently, milling the volume 13.3 μm × 8.0 μm × 12.6 μm, on the top part of the pillar; Figure S21 (Supporting Information) shows SEM images of the first and last milled sections.

Via FIB-SEM tomography, a 3D volume of three phases was reconstructed: Figure 5g shows the distribution of three phases, and Figure 5h shows pore distribution, and lastly, Figure 5i shows the distribution of effective TPBs within the analyzed volume of pillar structure. The parameters calculated through the 3D reconstruction are listed in **Table 1**. Each parameter obtained from different volumes are listed in Table S2 (Supporting Information).

Considering the molar volume change from NiO to Ni is ca. 44%,[24] the estimated Ni volume fraction in pillars before sintering was 49.2%, which was similar to the volume fraction of YSZ to NiO in the ink (47.8:52.2), and the volume change of NiO to Ni was the same as the pore volume fraction measured by FIB-SEM tomography. Hence, the volume ratio between YSZ and Ni remained the same as in the formulated NiO-YSZ ink, thereby successfully demonstrating its reliable printing of Ni-YSZ composite structures. The homogeneous distributions of Ni and YSZ within the printed pillar structure were also confirmed by SEM-energy dispersive X-ray spectroscopy (EDS), as shown in Figure S22 (Supporting Information).

As the diameter of the tested cell was larger (25 μm) than that in the previously calculated model, and the tortuosities (Table 1) were obtained from the printed pillar structure, the computational predictions of SOER performances were updated, with results shown in Figure 5j. The updated simulation showed a slight enhancement in SOFC performance with 97% H_2 as the pillar diameter was increased and the tortuosity was changed (Table 1). In SOE mode with just 24% steam fed to negative electrodes, current densities also increased slightly, but still increasing pillar height caused decreased power densities and severe performance saturation, due to reactant depletion through the porous Ni-YSZ structure, as shown in Figure 5k. Increasing steam content to 80% relaxed performance limitation evident with 24% steam. The plotted data (Figure S23, Supporting Information) also demonstrated that in electrolysis mode, increasing pillar height led to a decrease in up-scaling factor; the most effective SOER pillar height depends on gas compositions. The distribution of the reactant (steam) was predicted with the model of different pillar heights (70, 150, and 190 μm) and is shown in Figure S24 (Supporting Information). Compared to the reactant distribution in the 70 μm pillar, the distribution in the 150 and 190 μm pillars exhibited severe depletion within the cell, which supports the results in Figure 5j.

Table 2. TEC values of the materials used in the SOERs layer components.

	Material	Thermal expansion coefficient (x 10^{-6} K^{-1})	Ref
Positive electrode	$La_{0.8}Sr_{0.2}MnO_3$	11.3	[25]
Electrolyte	YSZ	10.5	[26]
Negative electrode	Ni-YSZ (40 wt% Ni)	10–12.5	[27]
	NiO-YSZ (14% porosity)	11.88	[26]

Lastly, to evaluate the durability of printed pillars and their suitability for application to commercial large-size cell, the thermal expansion coefficient (TEC) values of the materials in each component were investigated. A high TEC mismatch can result in internal stresses, potentially leading to delamination or cracking of the cell. **Table 2** lists the TECs of the materials in each part of the cell, showing TEC values in the range of 10–12.5, including both Ni-YSZ and NiO-YSZ. This implies that during sintering and operation, high thermal stresses were not expected to be caused by TEC mismatches, suggesting suitability of those materials for reactor durability and for its application in large-size cells.

Additional discussion regarding the sintering process for the large-sized planar cell with pillar structures is included in the supplementary information. This section presents a proposed design of the pillar array on the surface and an alumina setter plate for sintering (Figure S25, Supporting Information), addressing its feasibility for application in large-scale reactors.

3. Conclusion

Ni(O)-YSZ and YSZ pillars were successfully 3D inkjet printed on to planar Ni(O)-YSZ substrates, to extend electrode | electrolyte areas, thereby up-scaling SOERs. Dip-coating was used to deposit YSZ on Ni(O)-YSZ pillars, then sintered and dip-coated LSM positive electrodes applied, followed by sintering. The performance of those cells was compared with those fabricated with YSZ pillars. For both types of structures, effects of current density, pillar

© 2024 The Authors. Small published by Wiley-VCH GmbH
RIGHTSLINK
16136829, 2024, 40, Downloaded from https://onlinelibrary.wiley.com/doi/10.1002/smll.202306653 by Imperial College London, Wiley Online Library on [22/10/2024]. See the Terms and Conditions (https://onlinelibrary.wiley.com/terms-and-conditions) on Wiley Online Library for rules of use; OA articles are governed by the applicable Creative Commons License

heights and temperature on cell potential differences were determined in (H_2 and air) fuel cell and (steam and CO_2) electrolyzer modes.

As predicted by finite element simulations, in fuel cell mode, cells with 40 µm Ni-YSZ pillars produced peak power density enhancement by a factor of 3.4 when compared to planar structures, whereas cells with YSZ pillars increased peak power densities by a factor of only 1.82. In steam electrolysis mode, at the thermoneutral potential of 1.285 V, cells with Ni-YSZ pillars doubled current densities compared to values with planar cells; in CO_2 electrolysis mode, current densities in such cells were increased by ca. 1.97 compared with planar cells. FIB-SEM 3D tomography on tops of Ni-YSZ pillars showed the same phase ratio as those of inks used in their printing, showing high TPBs densities and homogeneous spatial distributions of Ni and YSZ phases.

Though increased pillar heights were predicted to increase upscaling factors, and fabrication of cells with taller (> 100 µm) pillars was achieved, subsequent use of dip-coating to deposit YSZ electrolytes and/or LSM-YSZ positive electrodes led to inhomogeneous spatial distributions of those phases and their subsequent cracking. Hence, 3D printing followed by coating methods such as aerosol deposition that can evenly coat thin electrolyte layers on the pillars is recommended.

4. Experimental Section

Fabrication of Negative Electrode Support Layers: As described previously,[4b] negative electrode support layers were prepared by the pelletization method. NiO (NiO-S, Fuelcellmaterials, USA) and YSZ (8YSZ-U5, Fuelcellmaterials, USA) powders were mixed in ethanol with carbon particles (Sigma Aldrich, USA) as a pore former at concentrations of 10 wt.% ratio to the ceramic powders. The mixed dispersion was ball-milled for 24 h using zirconia balls and then dried at 70 °C for 24 h. The dried powders were lightly ground and then pressed into a 25 mm diameter size pellet at 10 MPa pressure, using a pellet press die set (Specac Ltd, UK). The pressed NiO-YSZ pellets were heat treated ultimately at 900 °C for 5 h, with 1-hour interval heat treatment at 450 °C to combust residual organics.

Ink Preparation and Its Analysis: YSZ and Ni(O)-YSZ composite inks were prepared for the pillar-structured YSZ electrolyte layer printing and the pillar-structured Ni(O)-YSZ functional layer printing, respectively. YSZ ink was prepared by dispersing commercial YSZ powders (8YSZ-U1, Fuel cell materials, USA) in de-ionized (DI) water adding Dispex A40 (Ciba-BASF, UK), PEG-35000, and Natsurf (Croda Chemicals, UK) as dispersant, binder, and surfactant, respectively. The YSZ ink preparation has been described previously.[12]

For formulation of NiO-YSZ inks, NiO and YSZ particles were mixed in 1:1 weight ratio and the particles were dispersed in the DI water with a 32 wt.% ratio to the solvent. The dispersant ratio (dispersant weight to the total surface area of the particles) in NiO-YSZ inks was varied from 0.2 to 7 mg m^{-2}, to determine its effect on ink particle size and zeta potential. The ratio was fixed at 2 mg m^{-2} at which effective particle sizes were smallest (D50: 540 nm) and zeta potentials exhibited their most negative values (−39 mV). To break particle agglomerates, Ni(O)-YSZ particles were dispersed by ball-milling using a mixture of 3 mm and 5 mm size zirconia balls for 24 h on electrically-driven cylindrical rollers. Then the ink was centrifuged at 1400 rpm for 2 min, and 1000 rpm for 5 min, subsequently. After filtering the ink using an 800 nm pore-size sterile syringe filter (Cole-Parmer, UK), the particle weight ratio of ink was measured. PEG-35000 was added with a 25 mg cm^{-3} ratio (binder weight to ink volume) and mixed for another 24 h using a magnetic stirrer. Natsurf 265 (Croda Chemicals, UK) was added at a concentration of 2.5 mg cm^{-3} just before starting the printing to increase the ink stability to aggregation.

The viscosities and surface tensions of inks were measured respectively using a rheometer and drop shape analyzer (DSA 25S, KRÜSS, Germany) to evaluate their suitability for inkjet printing. Dispersed particle sizes were measured using a particle size analyzer (Mastersizer 2000, Malvern Panalytical, UK).

Fabrication of Pillared Structured Cells: Ni(O)-YSZ pillars were first printed on the Ni(O)-YSZ pre-sintered negative electrode support layer by a 3D inkjet printer (X-serie, Ceradrop, France). For the YSZ pillars, the printing was done on the surface of a dip-coated YSZ electrolyte layer that was not yet sintered. As prepared YSZ inks or Ni(O)-YSZ inks were filtrated using an 800 nm syringe filter before filling a DMC ink cartridge (DMC, Fujifilm, Japan). Ceraprint software was used to design a rectangular pillar array with a 50 µm diameter and 80 µm spacing between each pillar. The height of pillars was controlled by varying the number of printing layers. At every ten layers, the printing was paused, and purging was conducted to avoid the nozzle clogging during printing. After completion of the printing, printed pillars were heat-treated at 600 °C for 1 h, with 450 °C intermediate heat-treatment for 1 h to remove the organic materials remaining in the ink and provide a slight interconnection between the printed Ni(O)-YSZ pillars and the negative electrode support substrate.

The YSZ layer was dip-coated on the Ni(O)-YSZ structures to cover the entire pillar structure homogeneously, and then it was heat-treated at 600 °C again for the same purpose. The one-side dip-coating process has been reported previously.[28] After the 600 °C heat treatment, the cell was sintered at 1450 °C for 5 h to obtain a fully dense YSZ layer.

After the YSZ sintering step, the LSM-YSZ layer was applied to the YSZ electrolyte surface also using the dip-coating method for the homogeneous distribution of the positive electrode layer on the electrolyte layer. Subsequently, the LSM-YSZ layer was dried at 70 °C for 1 h and then heat treated at 1000 °C for 2 h.

All particle size information for the materials used, as well as details about the sintering and heat-treatment conditions, are organized in a table in the Tables S3 and S4 (Supporting Information).

Additionally, for a comprehensive understanding of the entire experimental process, an overview is provided through a schematic illustration in Figure S26 (Supporting Information).

Electrochemical Performance Analysis: The fabricated cells were attached using ceramic adhesive (Ceramabond 668, Aremco, USA) to an alumina tube which had a 25 mm outer diameter and 20 mm inner diameter, and inserted into a vertical tube furnace (TS1 12/60/300, Carbolite-Gero, UK). A potentiostat/galvanostat (PGSTAT302N, Ecochemie, Metrohm, The Netherlands) was used in two electrode mode, connected to cells using Ag and Pt wires, with separate wires for measurement of potential differences and currents, This enabled their current density-potential difference performance to be measured at 700, 750, and 800 °C, as well as characterized by electrochemical impedance spectroscopy (EIS) in the frequency range of 105–0.1 Hz.

Fuel cell performance was measured with the air gas flow of 200 standard cubic centimetres per minute (sccm) on the positive electrode side and hydrogen (+ 3% H_2O) gas flow of 100 sccm on the negative electrode side. Electrolysis performance was tested with the same air gas flow, but on the negative electrode side, 24% steam was fed with a carrier gas flow rate of 50 sccm for each H_2 and Ar gas. Steam was generated using vapour generator (CEM, W-101A, Bronkhorst, Netherland) with a steam generation temperature at 100 °C.

For CO_2 electrolysis, mixtures of CO and CO_2 gas were fed to the Ni-YSZ electrode side with CO_2 to CO ratios: CO_2: CO = 30: 70, 50: 50, 70: 30, and a total gas flow of 100 sccm. Dry H_2 was fed with 10 sccm flow rate to prevent oxidation of Ni in the negative electrode support layer side.

The schematic illustration, which outlines the experimental setup for electrochemical performance testing, is included in Figure S27 (Supporting Information).

Microstructure Analysis and 3D Reconstruction: The structure of printed pillars was observed first by an optical microscope (OM, GXM-L3230, GT vision, UK) to confirm the ink properties for printing and printed microstructures immediately after printing. The microstructure of fabricated pillars after sintering and their cross-section images were analyzed using a scanning electron microscope (SEM, Zeiss Leo Gemini 1525, Germany).

© 2024 The Authors. Small published by Wiley-VCH GmbH
RIGHTSLINK
16136829, 2024, 40, Downloaded from https://onlinelibrary.wiley.com/doi/10.1002/smll.202306653 by Imperial College London, Wiley Online Library on [22/10/2024]. See the Terms and Conditions (https://onlinelibrary.wiley.com/terms-and-conditions) on Wiley Online Library for rules of use; OA articles are governed by the applicable Creative Commons License

The tortuosity and porosity of the reduced Ni-YSZ pillar structures were obtained by 3D reconstruction of the images obtained using focused ion beam-SEM (FIB-SEM, Auriga, Zeiss, Germany), followed by an analysis with a MATLAB plug-in application.[29] For cutting into cell microstructures, first 16 nA current was used for rough cutting and then gradually decreased from 4 nA (30 kV) to 1 nA (30 kV) to produce smoother cut end surfaces. For slicing the volume 13.3 µm × 8.0 µm × 12.6 µm, a current of 240 nA (30 kV) was used, and the image of each sliced section was stored after each slicing step. Avizo software was utilized for 3D reconstruction of microstructures using the acquired images.

Supporting Information

Supporting Information is available from the Wiley Online Library or from the author.

Acknowledgements

The authors thank Shell Global Solutions International B.V for a research contract providing post-doctoral research associateships for I.J.

Conflict of Interest

The authors declare no conflict of interest.

Data Availability Statement

The data that support the findings of this study are available from the corresponding author upon reasonable request.

Keywords

3D micro-structured functional layer, CO_2 electrolysis, inkjet 3D printing, solid oxide electrolyser, solid oxide fuel cell

Received: August 3, 2023
Revised: March 8, 2024
Published online: March 27, 2024

[1] a) G. Glenk, S. Reichelstein, *Nat. Commun.* **2022**, *13*, 2010; b) A. Hauch, R. Küngas, P. Blennow, A. B. Hansen, J. B. Hansen, B. V. Mathiesen, M. B. Mogensen, *Science* **2020**, *370*, eaba6118; c) Z. Shao, S. M. Haile, J. Ahn, P. D. Ronney, Z. Zhan, S. A. Barnett, *Nature* **2005**, *435*, 795; d) S. J. Davis, N. S. Lewis, M. Shaner, S. Aggarwal, D. Arent, I. L. Azevedo, S. M. Benson, T. Bradley, J. Brouwer, Y.-M. Chiang, *Science* **2018**, *360*, eaas9793.

[2] a) T. A. Schmauss, S. A. Barnett, *ACS Energy Lett.* **2021**, *6*, 3180; b) F. Baldi, L. Wang, M. Pérez-Fortes, F. Maréchal, *Front. Energy Res.* **2019**, *6*, 139.

[3] a) M. Lamagna, B. Nastasi, D. Groppi, C. Rozain, M. Manfren, D. A. Garcia, *Energy Convers. Manage.* **2021**, *235*, 113993; b) M. Mogensen, M. Chen, H. Frandsen, C. Graves, J. Hansen, K. Hansen, A. Hauch, T. Jacobsen, S. Jensen, T. Skafte, *Clean Energy* **2019**, *3*, 175; c) S. H. Jensen, C. Graves, M. Mogensen, C. Wendel, R. Braun, G. Hughes, Z. Gao, S. A. Barnett, *Energy Environ. Sci.* **2015**, *8*, 2471.

[4] a) J. An, Y.-B. Kim, J. Park, T. M. Gür, F. B. Prinz, *Nano Lett.* **2013**, *13*, 4551; b) I. Jang, G. Kelsall, *Electrochem. Commun.* **2022**, *137*, 107260; c) Y. Xu, F. Tsumori, T. Osada, H. Miura, *Nano Lett* **2013**, *8*, 571; d) A. Pesce, A. Hornés, M. Núñez, A. Morata, M. Torrell, A. Tarancón, *J. Mater. Chem. A* **2020**, *8*, 16926.

[5] I. Jang, J. Alexander, N. Farandos, G. Kelsall, *Electrochim. Acta* **2022**, *427*, 140902.

[6] G. H. McKinley, M. Renardy, *Phys. Fluids* **2011**, *23*, 127101.

[7] a) S. Kawale, I. Jang, N. Farandos, G. H. Kelsall, *React. Chem. Eng.* **2022**, *7*, 1692. b) B. Derby, *J. Eur. Ceram. Soc.* **2011**, *31*, 2543.

[8] a) B. Derby, N. Reis, *MRS Bull.* **2003**, *28*, 815; b) D. Corzo, K. Almasabi, E. Bihar, S. Macphee, D. Rosas-Villalva, N. Gasparini, S. Inal, D. Baran, *Adv. Mater. Technol.* **2019**, *4*, 1900040.

[9] D. Jang, D. Kim, J. Moon, *Langmuir* **2009**, *25*, 2629.

[10] B. Derby, *Annu. Rev. Mater. Res.* **2010**, *40*, 395.

[11] G. Cummins, M. P. Desmulliez, *Circuit World* **2012**, *38*, 193.

[12] N. Farandos, I. Jang, J. Alexander, G. Kelsall, *Electrochim. Acta* **2022**, *426*, 140834.

[13] J. Richardson, D. Yiagas, B. Turk, K. Forster, M. Twigg, *J. Appl. Phys.* **1991**, *70*, 6977.

[14] a) R. D. Deegan, O. Bakajin, T. F. Dupont, G. Huber, S. R. Nagel, T. A. Witten, *Nature* **1997**, *389*, 827; b) M. Mikolajek, A. Friedrich, W. Bauer, J. Binder, presented at Ceram. Forum Int **2015**, *92*, E25.

[15] a) M. Majumder, C. S. Rendall, J. A. Eukel, J. Y. Wang, N. Behabtu, C. L. Pint, T.-Y. Liu, A. W. Orbaek, F. Mirri, J. Nam, *J. Phys. Chem. B* **2012**, *116*, 6536; b) Y. Li, C. Diddens, T. Segers, H. Wijshoff, M. Versluis, D. Lohse, *Proc. Natl. Acad. Sci. USA* **2020**, *117*, 16756.

[16] A. J. Martín, G. O. Larrazábal, J. Pérez-Ramírez, *Green Chem.* **2015**, *17*, 5114.

[17] J. B. Hansen, *Faraday Discuss.* **2015**, *182*, 9.

[18] Z. Yan, J. L. Hitt, J. A. Turner, T. E. Mallouk, *Proc. Natl. Acad. Sci. USA* **2020**, *117*, 12558.

[19] I. Jang, S. Kim, C. Kim, H. Lee, H. Yoon, T. Song, U. Paik, *J. Power Sources* **2019**, *435*, 226776.

[20] M. P. Albano, L. B. Garrido, *Ceram. Int.* **2013**, *39*, 29.

[21] a) R. Sathyanath, A. Aarthi, S. K. Kalpathy, *Chem. Eng. Sci.* **2020**, *218*, 115552; b) C. Xia, S. Zha, W. Yang, R. Peng, D. Peng, G. Meng, *Solid State Ionics* **2000**, *133*, 287.

[22] K. Cook, J. Wrubel, Z. Ma, K. Huang, X. Jin, *J. Electrochem. Soc.* **2021**, *168*, 114510.

[23] K. Chen, *Int. J. Hydrogen Energy* **2011**, *36*, 10541.

[24] S. De Angelis, P. S. Jørgensen, E. H. R. Tsai, M. Holler, G. Fevola, J. R. Bowen, *Mater. Charact.* **2020**, *162*, 110183.

[25] M. Mori, Y. Hiei, N. M. Sammes, G. A. Tompsett, *J. Electrochem. Soc.* **2000**, *147*, 1295.

[26] M. Mori, T. Yamamoto, H. Itoh, H. Inaba, H. Tagawa, *J. Electrochem. Soc.* **1998**, *145*, 1374.

[27] D. Osinkin, D. Bronin, S. Beresnev, N. Bogdanovich, V. Zhuravlev, G. Vdovin, T. Demyanenko, *J. Solid State Electrochem.* **2014**, *18*, 149.

[28] I. Jang, C. Kim, S. Kim, H. Yoon, *Electrochim. Acta* **2016**, *217*, 150.

[29] S. J. Cooper, A. Bertei, P. R. Shearing, J. Kilner, N. P. Brandon, *SoftwareX* **2016**, *5*, 203.

© 2024 The Authors. Small published by Wiley-VCH GmbH

RIGHTSLINK

16136829, 2024, 40, Downloaded from https://onlinelibrary.wiley.com/doi/10.1002/smll.202306653 by Imperial College London, Wiley Online Library on [22/10/2024]. See the Terms and Conditions (https://onlinelibrary.wiley.com/terms-and-conditions) on Wiley Online Library for rules of use; OA articles are governed by the applicable Creative Commons License